

# Processing, microstructural evolution and strength properties of in-situ magnesium matrix composites containing nano-sized polymer derived SiCNO particles

Nagaraj M. Chelliah<sup>a</sup>, Harpreet Singh<sup>a,\*</sup>, Rishi Raj<sup>c</sup>, M.K. Surappa<sup>b</sup>

<sup>a</sup> Department of Mechanical Engineering, Indian Institute of Technology Ropar, Rupnagar 140001, Punjab, India

<sup>b</sup> Department of Materials Engineering, Indian Institute of Science, Bengaluru 560012, Karnataka, India

<sup>c</sup> Department of Mechanical Engineering, University of Colorado Boulder, Boulder 80309, CO, USA

## ARTICLE INFO

### Keywords:

Magnesium  
Polymer derived ceramics  
In-situ composites  
Castings  
Friction stir processing

## ABSTRACT

In-situ Mg matrix composites are fabricated by combining both liquid- and solid-state processing routes. Firstly, liquid polymer was injected into the molten Mg at a temperature of 800 °C to initiate pyrolysis. In-situ pyrolysis aids in the conversion of liquid polymer into sub-micron sized SiCNO particles (mean particle size in the range of 0.5–1 μm) and Mg<sub>2</sub>Si particles. Most of the polymer derived SiCNO particles were pushed by the solidification front and as a result segregated at the grain boundaries of as-cast composites (mean grain size in range of 50–65 μm) during subsequent solidification process. Formation of Mg<sub>2</sub>Si phase could be minimized by reducing the pyrolysis temperature from 800 to 700 °C. Single pass friction stir processing (FSP) of these as-cast composites lead to improved homogeneity in the SiCNO particle distribution, particle refinement (mean particle size of about 200–300 nm) and grain refinement (mean grain size in range of 2.5–3.5 μm). Mechanical properties (hardness, compressive yield stress, ultimate compressive stress, strain to failure and strain hardening exponent) of the FS processed composites were enhanced significantly as compared to their as-cast counterparts. Strengthening mechanisms and numerical models are being evoked to explain the observed yield strength in these two stage processed composites.

## 1. Introduction

Magnesium metal matrix composites (MMMCs) have significant potential in the design and manufacturing of next generation automotive and aerospace vehicles having light weight and reduced fuel consumption [1,2]. In-situ composite fabrication techniques seem to be gaining attraction since it overcomes several issues (non-uniformity of particle distribution, poor wettability and weak interfaces) associated with composites produced by conventional processing techniques [3,4]. In general, in-situ MMCs consist of ultra fine-sized and thermodynamically stable ceramic particles, clean and unoxidized ceramic-metal interfaces with high interfacial strength, due to improved wettability. There exist several variants of in-situ processes. These include both liquid metallurgy, and solid state processing routes [5–10]. Bhingole [7] added magnesium nitrate as oxygen supplying agent into the molten Mg-alloy and synthesized in-situ AZ91 matrix composites by in-situ reactive formation of hard MgO and Al<sub>2</sub>O<sub>3</sub> particles. Despite the fact that numerous in-situ MMC processing routes are reported in the literature [5–10], their reaction pathways and chemical kinetics are

complex to understand. Sudarshan et al. [11,12] developed a novel processing route to synthesize in-situ Mg-based MMCs by utilizing pyrolysis of polymer precursor within the molten Mg. Since polymer precursor contain all the constituents of ceramic phases within organic molecules itself, an in-situ pyrolysis aids in the conversion of polymer into ceramic particles without any chemical reaction between precursor and the host metal. However, they indentified two critical processing issues [11,12]: firstly the reaction between polymer precursor and magnesium melt results in the formation of brittle Mg<sub>2</sub>Si particles at pyrolysis temperature ranging from 800 to 1000 °C. This brittle Mg<sub>2</sub>Si phase impairs the ductility of resulting composite. Further, this leads to the reduction in the amount of polymer precursor available for generation of sub-micron sized SiCNO particles. Secondly, most of the polymer derived ceramic (PDC) particles were pushed away by the solidification front and as a result segregated at the grain boundaries. Such grain boundary segregation limits the enhancement in the mechanical properties of the final in-situ MMCs.

The nature and magnitude of interactive force between the ceramic particles and solidification front determines the nature of particle

\* Corresponding author.

E-mail address: [harpreetsingh@iitrpr.ac.in](mailto:harpreetsingh@iitrpr.ac.in) (H. Singh).

distribution in the final MMCs [13]. If the net force is attractive, the particles could be trapped within grain resulting in uniform dispersion where as repulsive forces leads to segregation of particles at the grain boundaries. Rapid solidification processing [14] and disintegrated melt technique [15] minimize the grain boundary segregation due to higher cooling rate to certain extent; however, it is difficult to understand and control the nature of interactive forces, and the solidification variables precisely during large-scale manufacturing of cast composites. Secondary process such as hot extrusion is more often used to bring about uniformity in particle distribution and to eliminate /minimize casting defects in the composites [16]. However, under non optimal conditions this may lead to some level of texture and anisotropy in the particulate MMCs.

In the present investigation, friction stir processing (FSP), one of the well-established solid state processing technique [17] has been explored as a technique to achieve both grain refinement and uniform distribution of reinforced particle distribution in the cast composites. These improvements have accrued due to intense material flow and dynamic recrystallization (DRX) which are the main attributes of FSP. Therefore, FSP can be utilized to minimize the grain boundary segregation of particles in the as-cast in-situ MMCs. In addition, FSP can also be used to eliminate/minimize casting defects akin to hot-extrusion process. Arora et al. [18] observed the formation of in-situ nano-particles during FSP of AE42 Mg-alloys. Ranjit [19] modified the as-cast microstructures of Al-TiC in-situ composites by FSP. Ajay et al. [20] achieved a five-fold increase in microhardness of Cu-based in-situ MMCs after introducing polymer precursor by multi-pass friction stir processing (FSP). In their work, since the pyrolysis temperature (800 °C) of polymer precursor is lower than the melting temperature of Cu matrix (1083 °C); in-situ pyrolysis can be performed by solid state FSP itself. However, for the case of Mg, liquid state processing is required to initiate the pyrolysis for the conversion of polymer in to ceramic phase as pyrolysis temperature (700–800 °C) is greater than the melting temperature of Mg (650 °C). Use of FSP process has not been reported for the light weight in-situ MMCs dispersed with polymer derived ceramic (PDC) particles to the best of our knowledge. The primary objective of the present paper is three-fold; (i) to minimize the formation of Mg<sub>2</sub>Si phase by lowering the process or pyrolysis temperature, and (ii) to achieve the uniform dispersion of PDC particles throughout the magnesium matrix via FSP and (iii) to investigate the microstructural evolution, strength properties and the basis of strengthening of two stage processed in-situ MMCs.

## 2. Experimental methods

### 2.1. Matrix materials and polymer precursors

Commercially grade Mg(99.9%) billets (supplied from Hindustan Aerospace limited, Bengaluru) was chosen as the matrix material. Poly(urea-methyl-vinyl)silazane (PUVMS) procured from Kion Corporation (USA), was utilized as polymer precursor for the reinforcement. As received liquid polymer was introduced directly into the molten Mg in all the casting experiments. Direct injection of liquid polymer helped in saving consumption of additional energy and also time involved in polymer cross-linking, and ball milling of cross-linked precursor.

The weight fraction of liquid polymer to be added into molten Mg is estimated based on the following formula;

$$W_f^{\text{precursor}} = \frac{\rho_{\text{PDC}}}{0.65\rho_{\text{Mg}}} V_f^{\text{PDC}} \quad (1)$$

The factor of 0.65 indicates the ceramic yield from the liquid polymer which was determined experimentally.

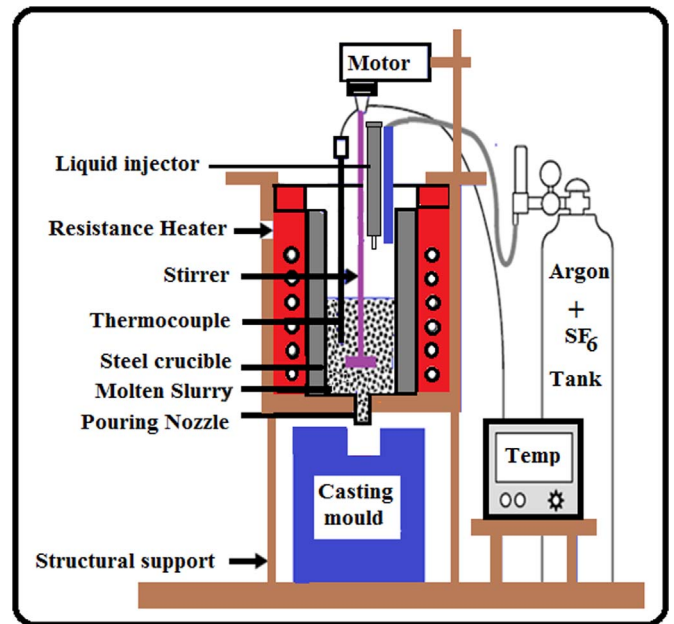


Fig. 1. Schematic diagram of furnace used for fabricating in-situ Mg MMCs.

### 2.2. Two step processing of composites (combination of liquid and solid state)

For the first time two-step process has been employed in processing of Mg MMCs containing nano-sized PDC particles. Two-step process consists of primary processing of magnesium MMCs through in-situ pyrolysis followed by friction stir processing. Two-step process employed in the present investigation attempts to mitigate critical issues associated with direct melt route in the following manner; (i) the intensity of Mg<sub>2</sub>Si formation is minimized by lowering the pyrolysis temperature from 800 °C to 700 °C (ii) The issue of grain boundary segregation can be reduced through FSP treatment. The severe plastic deformation within the nugget zone is expected to create fragmentation in the sub-micron sized SiCNO particles leading to nano-sized PDC particles, and stirring action arising during FSP tool aids in achieving the uniform dispersion of particles throughout the Mg matrix.

#### 2.2.1. In-situ processing

The schematic diagram of melting furnace used for fabrication of in-situ magnesium MMCs is shown in Fig. 1. 700 g of Mg blocks were melted in a steel crucible using an electrical resistance furnace at a temperature of 700 °C. The steel crucible was continuously purged with Ar-5%SF<sub>6</sub> gas mixture to eliminate the flammability and risk of fire hazards with molten Mg. The melt was mechanically stirred by a 3-axial stirrer blade at 600 rpm to create good vortex in the melt. Subsequently, 3.5 wt% liquid polymer was injected into the melt and the stirring was continued for next 15 min in order to ensure completion of pyrolysis. After processing, the mixed molten slurry was bottom-poured into a pre-heated rectangular split-molds made of steel. Temperature of the molds was kept at 300 °C. In-situ Mg MMC castings were also fabricated exactly in similar manner at 800 °C. Thus fabricated as-cast in-situ MMCs were designated as PL700 and PL800. Here, PL indicates composites fabricated by directly injecting liquid into molten magnesium and the last 3 digit number refers to the temperature of pyrolysis.

#### 2.2.2. Friction Stir Processing (FSP) of as-cast Mg MMCs

A single-pass FSP was performed on as-cast composites by computer controlled (CNC) three axial vertical-type milling machine. The as-cast plates (300 mm length×100 mm width×6.5 mm thickness) were initially placed, and fixed by fixtures. The cylindrical FSP tool

made of H-13 tool steel had a shoulder diameter of 20 mm, and pin diameter and height of 6.5 mm and 6 mm respectively. FSP was done at constant tool rotation of 1000 rpm with transverse linear speed of 20 mm min<sup>-1</sup> under ambient condition. Plunge depth of 6.1 mm was maintained. PL700 and PL800 in-situ as-cast MMCs were FS processed and were designated as FPL700 and FPL800, respectively.

### 3. Material characterization

Matrix grain sizes and distribution of PDC particles in both as-cast and FS processed composites were characterized by optical microscope (Leica DM2700, Germany), scanning electron microscope (JEOL JSM-6610LV, Japan) and transmission electron microscope (Tecnai T20, FEI Company). Various phases including Mg<sub>2</sub>Si intermetallic particles crystals were identified using X-ray Diffractometer (PANalytical, X'pert-Pro (MPD), Netherlands). Raman spectroscopy was performed using a Renishaw spectrometer (excitation source: Argon ion laser,  $\lambda=514$  nm; laser power: 15 mW; sample objective: 50X). Micro-hardness profiles across the section of the nugget zone in FS processed, and as-cast composites were measured obtained using Vicker's micro-hardness tester (Wilson Instrument, United Kingdom) at a load of 500 gf (4.9 N) for a dwell time of 15 s. In the present study, all the hardness measurements were made on the matrix of the composites, taking due care to avoid indentation on the dispersed ceramic particles. Each hardness value represents an average of six measurements done at different locations on the matrix. Scatter in the micro-hardness data falls within 4% of the mean value. Uni-axial compression tests were performed using Tinius Olsen mechanical testing machine to record the room temperature mechanical properties at a constant strain rate of 10<sup>-3</sup> s<sup>-1</sup>. Cylindrical specimens were machined from the center of as-cast composites as well as FS processed composites (along the longitudinal direction of the nugget zone) by electrical discharge machining (EDM). Compression specimen had a diameter of 4 mm, and 6.5 mm height. Values of reported mechanical properties are average of three compression tests.

### 4. Results

Thermogravimetric analysis (TGA curve) of the liquid polymer in Argon atmosphere is shown in Fig. 2. It shows that pyrolysis is almost completed at 900 °C and the measured ceramic yield is about 65%. Typical microstructures of the as-cast PL800 and PL700 specimens are depicted in Fig. 3. Mg matrix and reinforced PDC particles can be easily distinguished by color contrast: light gray areas (marked as A) and black color areas (indicated as B) refer to segregated PDC particles at the grain boundaries. Coarse Mg<sub>2</sub>Si particles having Chinese script

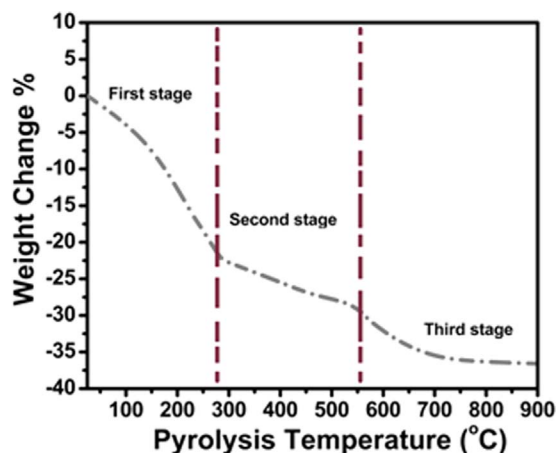


Fig. 2. Thermogravimetric analysis curve showing the pyrolysis reaction of liquid polymer in Argon atmosphere.

morphology (marked as C) is observed in as-cast PL800 specimen.

Microstructures of FPL800 and FPL700 composites are shown in Fig. 4. It is clear that distribution of fine-sized PDC particles is more uniform in the matrix of FS processed Mg composites, as shown in Figs. 4(a) and (b). It also can be seen that fragmented Mg<sub>2</sub>Si particles are redistributed more or less relatively uniform (Fig. 4(a)). The average grain size of as-cast composites is found to be in the range of 50–65  $\mu$ m whereas it was reduced to 2.5–3.5  $\mu$ m in the case of FS processed composites. The distribution of PDC particles at retreating and advancing zone of FSPed PL700 composite is illustrated in Fig. 5(a) and (b). As-cast PL800 specimen is characterized by grain boundary segregation of PDC particles, while FPL800 specimen shows uniform dispersion of the PDC particles throughout the Mg matrix (compare Fig. 6(a) and Fig. 6(b)). Fig. 7 illustrates the TEM micrograph of FS processed FPL700 composites indicating reasonable uniform dispersion of PDC (SiCNO) particles in the magnesium matrix. Microstructures of FS processed PL800 composite is shown in Fig. 8(a) and (b). XRD spectra shown in Fig. 9(a) indicate the presence of various phases in as-cast and FSPed composites. It is pertinent to mention that the peaks for SiCNO ceramic phases have not appeared in diffraction spectra as they are amorphous in nature. Raman spectra acquired from all the composites is shown in Fig. 9(b). It shows the existence of D and G peaks centered on 1325 and 1551 cm<sup>-1</sup>, respectively.

The hardness profiles of as-cast and FS processed PL700 specimens are shown in Fig. 10. Typical compressive true stress–true strain curves of in-situ composites and their corresponding strain hardening exponents are depicted in Fig. 11. Notice that compressive yield stress (CYS) of the fabricated composite is measured from yield point at which stress–strain curve becomes non-linear. It is evident that both hardness and CYS of FS processed composites are significantly higher when compared to those of as-cast composites (Fig. 10 and Fig. 11(a)). Fig. 12(a) shows the contribution of different strengthening mechanisms to the yield strength of processed composites based on strengthening mechanism models. A comparative analysis of various numerical models to predict yield strength of particulate MMCs is shown in Fig. 12(b).

### 5. Discussion

#### 5.1. In-situ pyrolysis of liquid polymer in Magnesium melts

As shown in Fig. 2, the polymer-to-ceramic conversion is a two-step process comprising of cross-linking and pyrolysis [21]. Initially, the viscosity of liquid polymer increases steadily to form rubber-like products at 250–280 °C [21]. The initial weight loss of 22% occurring between 25 and 280 °C can be ascribed to cross-linking process and this cross-linking primarily occurs due to the evaporation of low molecular weight oligomers via hydrosilylation, and transamination reactions [21]. Subsequently, 5% weight loss is observed between 280 and 550 °C due to the evolution of hydrocarbons and dehydrogenative coupling reactions [21]. The final weight loss is mainly associated with pyrolysis process which starts nearly at above 600 °C. During pyrolysis, H–C, Si–H and N–H bonds are broken within the polymer molecules to form covalent bonds between Si, C and N atoms. In the temperature range of 700–800 °C, the bonds between carbon and hydrogen become unstable and the hydrogen gas is released [21]. These dangling carbon atoms self-assemble into graphene-like network or retained as free carbon clusters [22]. After the complete conversion of polymer into ceramic phase, the PDC particles exhibit amorphous structures and this amorphous network consists of mixture of variety of covalent bonds between Si–C, Si–O, Si–N and C–C atoms [23]. As the final PDC contains certain level of residual oxygen, the general chemical composition of PDC particles can be denoted as SiC<sub>x</sub>N<sub>y</sub>O<sub>z</sub>. Raman spectroscopy is an effective tool to determine whether or not in-situ pyrolysis of liquid polymer within molten magnesium has led to the formation of PDC

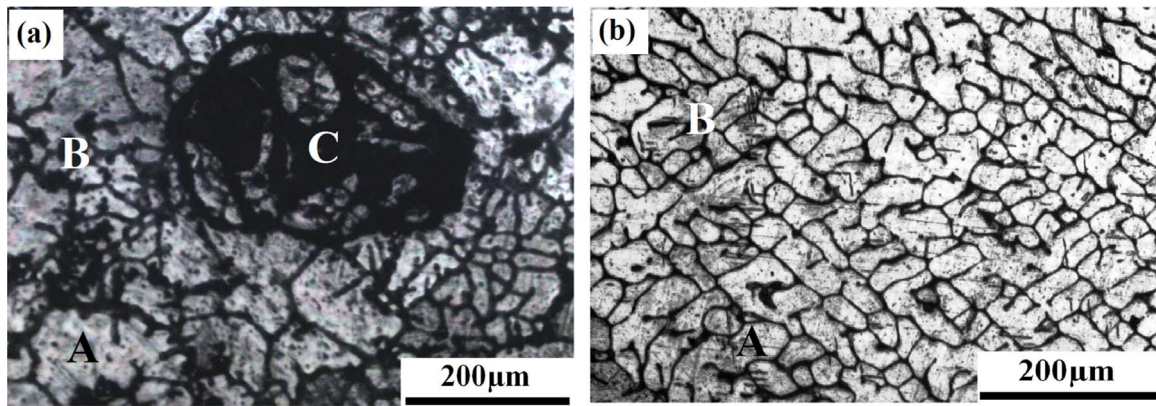


Fig. 3. Microstructures of Mg matrix reinforced with polymer derived ceramic particles (a) as-cast PL800 and (b) as-cast PL700 in-situ composites.

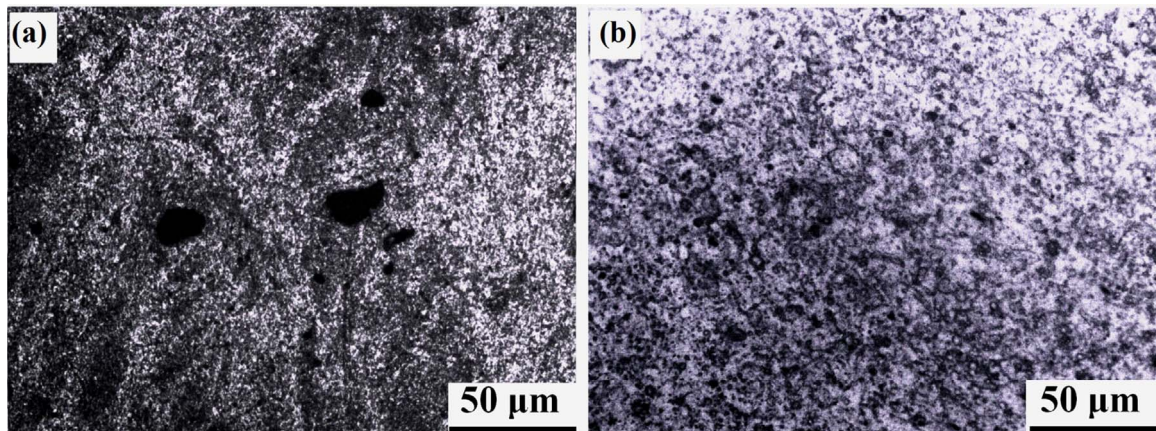


Fig. 4. Microstructures of Mg matrix reinforced with polymer derived ceramic particles (a) FS processed PL800 and (b) FS processed PL700 in-situ composites.

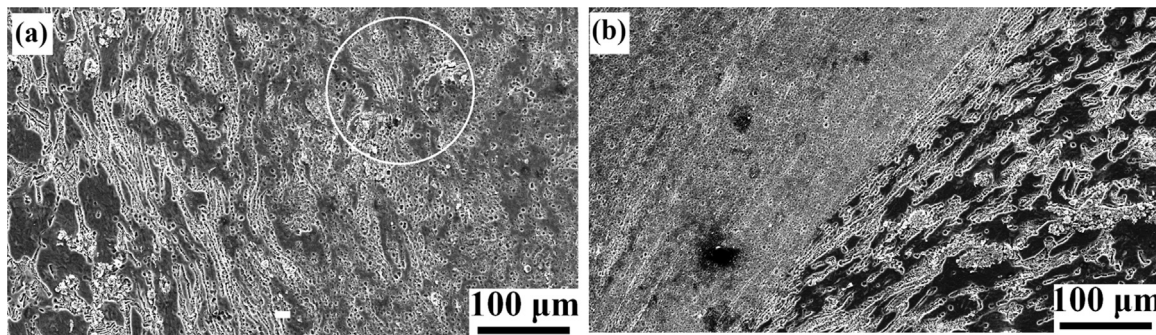


Fig. 5. SEM micrographs showing distribution of polymer derived particles in the Mg based in-situ composites (a) Retreating side and (b) Advancing side of FS processed PL700 composites.

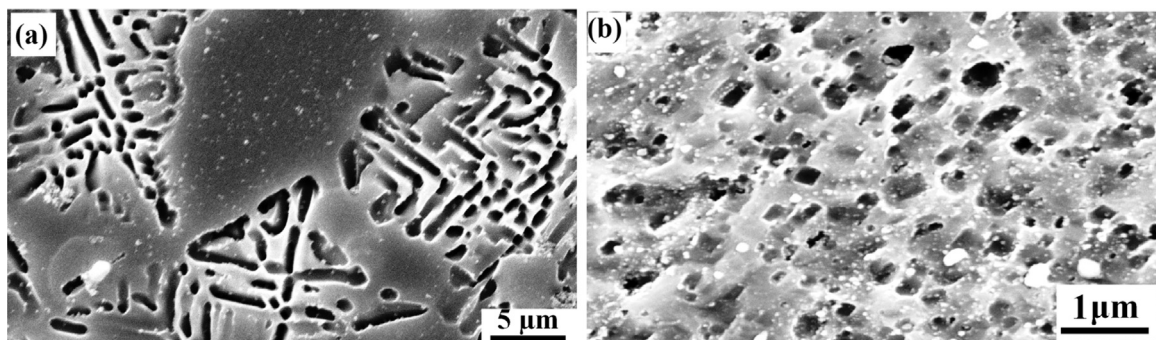


Fig. 6. SEM micrographs showing distribution of polymer derived particles in the Mg based in-situ composites (a) As-cast PL700 and (b) Nugget zone in FS processed PL700 composites.

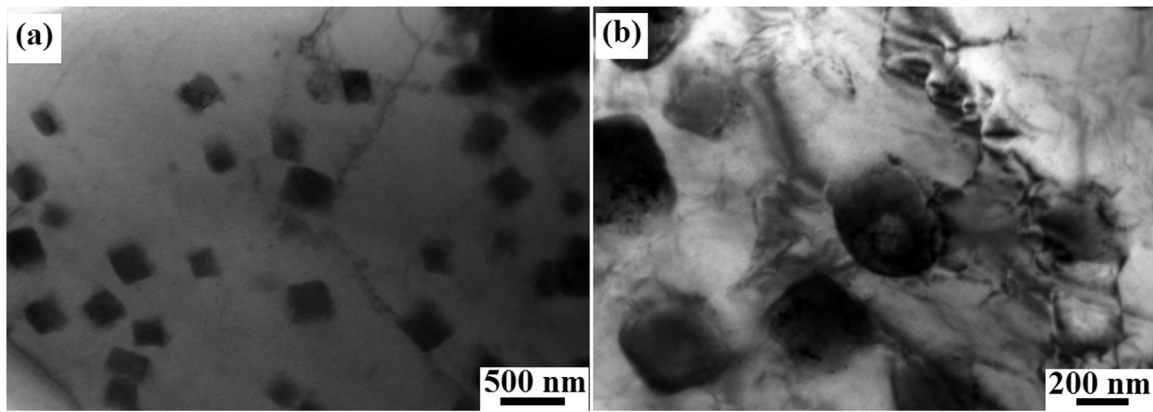


Fig 7. (a) and (b) TEM micrographs showing uniform distribution of polymer derived particles in the matrix of friction stir processed FPL700 in-situ composites.

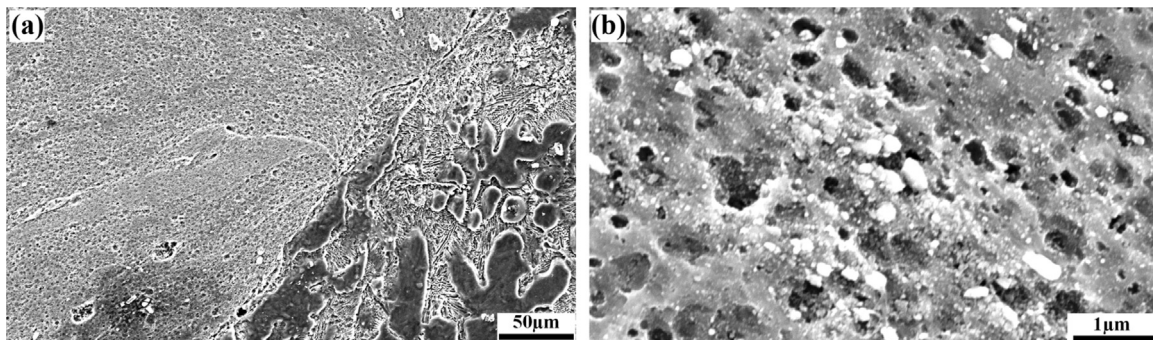


Fig. 8. SEM micrographs showing distribution of polymer derived particles in the Mg based in-situ composites (a) Advancing side of the FS processed PL800 and (b) Nugget zone in FS processed PL700 composites.

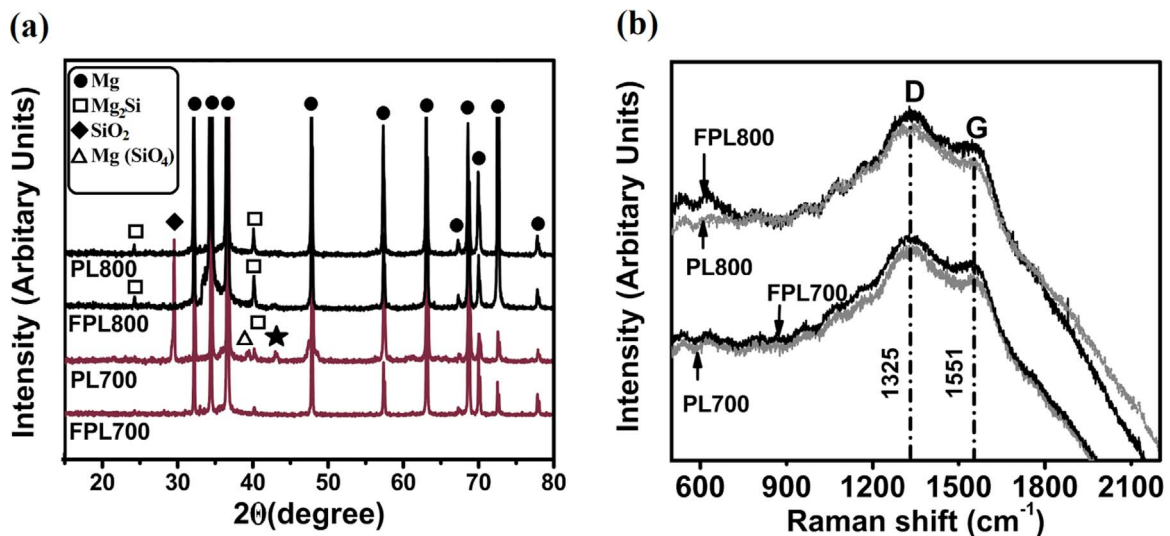


Fig. 9. (a) XRD patterns showing the presence of various phases (b) Raman spectroscopy data of as-cast and FS processed Mg based in-situ composites.

particles. For instance, Raman spectra give information about the conversion of  $sp^3$  carbon in the polymeric state into  $sp^2$  carbon in the ceramic state. The existence of D and G peaks is clear signature of the polymer-to-ceramic conversion as shown in Fig. 9(b). The D peak corresponds to the breathing mode of the  $sp^2$  rings whereas the G peak emerges from the stretching mode of the  $sp^2$  C–C bonds [22]. The overall relative intensities of these two peaks decrease with reduction in pyrolysis temperature from 800 to 700 °C. This means that pyrolysis intensity at 800 °C is slightly higher than at 700 °C. Further, the intensities of D and G peaks show negligible variation in the as-cast and FS processed composites. This suggests us that FSP does not alter the bonding characteristics of pyrolysed PDC particles. As shown in

Fig. 9(a), XRD spectra revealed two important features; (i) the intensity of  $Mg_2Si$  peaks appears to be stronger in composites processed at temperature of 800 °C and weak in composites processed at 700 °C, and (ii) the peaks of  $SiO_2$  and  $Mg(SiO_4)$  phases are apparent only in as-cast PL700 specimen, but such peaks are absent in FPL700 specimen. Owing to lower solubility of Si-atoms in the molten magnesium, Mg-atoms tend to react with Si-atoms to form an intermetallic phase of  $Mg_2Si$  crystal according to the following equation [24]:



Both at 800 °C and 700 °C, the change in Gibbs free energy values ( $\Delta G_f$ ) for the chemical reaction (1) are calculated to be  $-63.578$  kJ and

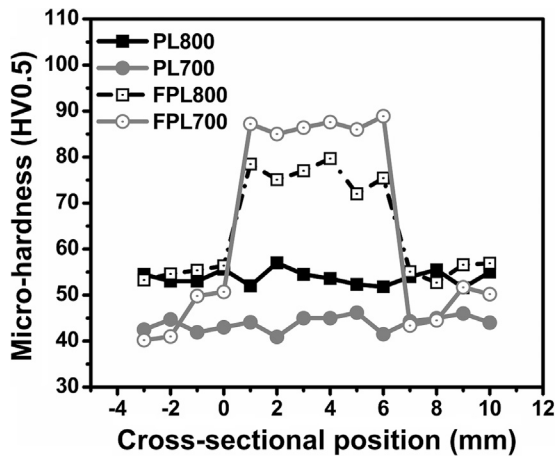
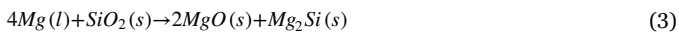


Fig. 10. (a) Microhardness profile of the investigated in-situ composites and (b) Tensile data.

–57.926 kJ, respectively. The higher negative value at  $\Delta G_f$  at 800 °C demonstrates that  $Mg_2Si$  formation occurs spontaneously at 800 °C as compared to that at 700 °C. In other words, the tendency towards  $Mg_2Si$  formation is minimized by lowering the pyrolysis temperature. Inem et al. [24] indentified the formation of  $Mg_2Si$  phases in the SiC particles reinforced AZ91 Mg-alloy composites. They reported that no extensive chemical reaction between Mg and SiC particle occurs at 900 °C. However,  $SiO_2$  scale which forms on SiC particle can react with molten Mg to form  $Mg_2Si$  according to the following chemical reaction.



This means that certain level of  $SiO_2$  scale is required to produce  $Mg_2Si$  particles in the composites. In the present work, XRD analysis confirmed that  $SiO_2$  peaks are present only in the PL700 specimen and absent in as-cast PL800 specimen. This points out that  $SiO_2$  phase was consumed completely in the PL800 composites due to the formation of  $Mg_2Si$  crystal whereas some free  $SiO_2$  is left behind in PL700 specimen due to lack of formation of  $Mg_2Si$  particles. Further, Lee et al. [25] reported that when AZ61 Mg-alloy is reinforced with nanoscale  $SiO_2$  particles by FSP,  $Mg_2Si$  and MgO phases are formed as result of chemical reaction (Eq. (3)) between nanoscale  $SiO_2$  particles and Mg in the alloy matrix. In this work, even though  $SiO_2$  particles are observed in the as-cast PL700 composite, such reaction has not taken place during FSP. This can be explained by the fact that nanoscale  $SiO_2$  particles having very high surface free energy, tend to be more

chemically active. This chemical reaction (Eq. (3)) is limited in FPL700 specimen due to the absence of nano-scale  $SiO_2$  particles. The fundamental reasons behind the existence of  $SiO_2$  and  $Mg(SiO_4)$  phases in the as-cast PL700 and their absence in the FPL700 specimen are not straight forward, and not clear at this stage. Nevertheless, the presence of these two phases is found to be necessary for the formation of  $Mg_2Si$  crystals [26].

### 5.2. Microstructural evolution

The striking difference in microstructures of the as-cast PL800 and as-cast PL700 composites is that the former exhibits bi-modal grain size distribution (Fig. 3(a)), whereas the latter shows more or less unimodal grain size distribution (Fig. 3(b)). The reason for such difference in microstructures is that PL800 contains both the SiCNO and  $Mg_2Si$  particles signifying higher amount of heterogeneous nucleation sites for producing Mg crystals. In the case of PL700 specimen mostly SiCNO particles with negligible amount of  $Mg_2Si$  particles are observed. This reduction in the amount of  $Mg_2Si$  particles (intensity of  $Mg_2Si$  peaks) in PL700 specimen could be verified from XRD spectra (Fig. 9(a)).

The typical basin type nugget of FS processed composites was observed in Fig. 5 as well as Fig. 8(a) and this is linked to the nature of material flow around the cylindrical tool used in the FS processing. Sato et al. [27] pointed out cylindrical-tool resulting in the generation of basin-shaped nugget zone in the upper zone due to maximum deformation and frictional heating during FSP using a cylindrical tool. On the retreating side of FS processed composite, the interface between nugget zone and thermo-mechanically affected (TMA) zone is relatively diffusive in nature with some evidence of vortex field as marked by circle in Fig. 5(a). However, the interface between advancing side of nugget and TMA zone is a quite sharp and consists of few layers of compacted ceramic particles aligned one over the other along the extruded direction as shown in Fig. 5(b). This is in consistent with the earlier reported results [28], where reinforced SiC particles are found to be aligned along deformation bands in AZ91 Mg-alloy composites. The width of this stacking zone of ceramic particles increases steadily as one moves towards the upper zone of the advancing front. This is associated with increase in the intensity of squeezing/extruding action, and frictional temperature towards the free surface of the advancing side. The microstructural differences between as-cast PL700 and FS processed PL700 is more clearly seen in Fig. 6(a) and (b). While the PDC particles in as-cast PL700 specimen as shown in Fig. 6(a) had a platelet morphology having a width of 0.5–1  $\mu m$  and length of 3–5  $\mu m$ .

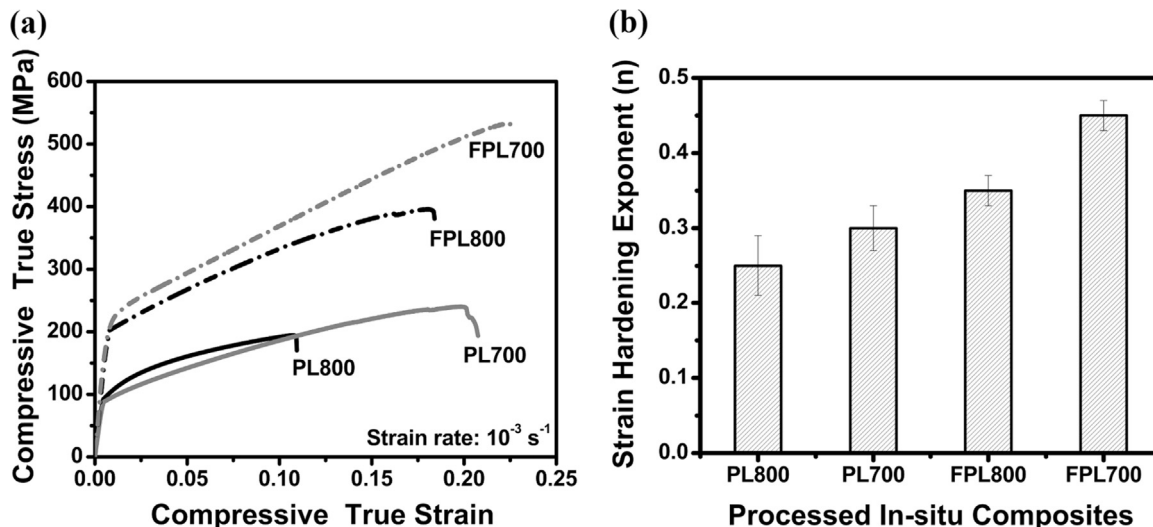


Fig. 11. Mechanical behavior of Mg based in-situ composites (a) Compressive stress-strain curves (b) Strain hardening response.

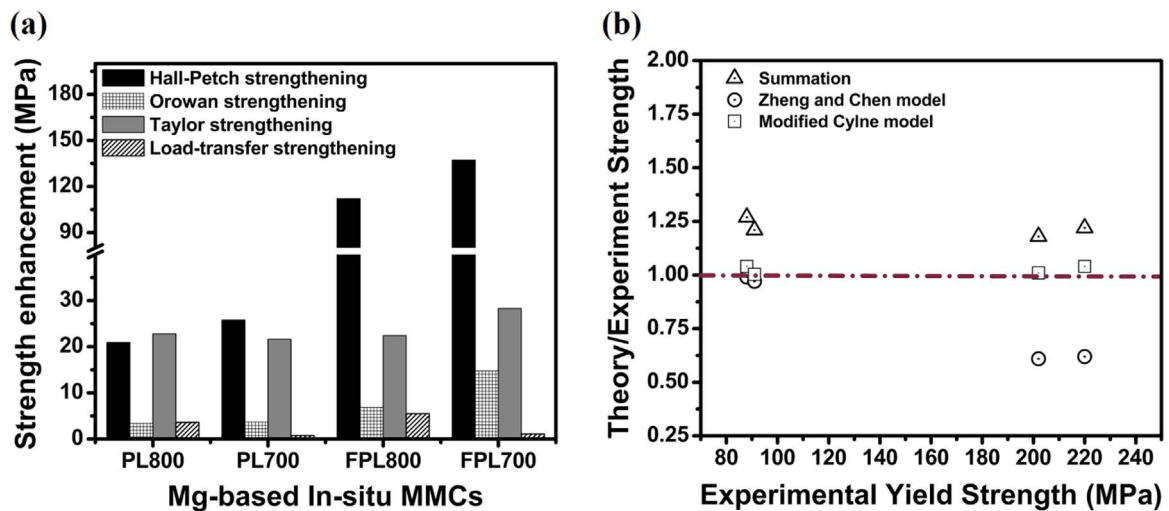


Fig. 12. (a) Influences of various strengthening mechanisms in Mg based in-situ composites and (b) Comparative analysis between numerical models and experimental data.

In contrast PDC particles in FS processed PL700 as seen in Fig. 6(b), seem to be near equiaxial shaped, and/or spherical morphologies with an average particle size in the range of 200–300 nm. It is evident that the refined PDC particles are redistributed uniformly throughout the nugget zone, and this is associated with severe plastic deformation during FSP. In addition, the uniform dispersion of PDC particles in the magnesium matrix of the FS processed FPL700 composites is further evident by TEM micrographs as shown in Fig 7. One can also clearly see the path profile of the material flow during FSP by observing the particle distribution pattern of PDC particles in the Mg matrix as they are chemically inert in nature. For instance, the uniformity of particle distribution is somewhat better in FPL700 as compared to that of FPL800 specimen. The interaction of Mg<sub>2</sub>Si particles with FSP tool may disrupt the path of material flow causing some amount of particle agglomeration in FPL800 specimen (Fig. 8(b)). The grain size refinement could be attributed to DRX process in the nugget zone during FSP (Figs. 4(a) and (b)). DRX process occurs by the progressive arrangement of dislocations around low-angle or high angle boundaries tending to form new grains. Depending on the friction temperature and strain rate experienced by the matrix material within nugget zone, variety of DRX microstructures (continuous DRX (CDRX) and discontinuous DRX (DDR)) are formed. The complete description of DRX microstructural evolution during FSP is beyond the scope of this paper and such information is available in earlier publications [29,30]. Watanabe et al. [31] proposed an empirical correlation between the final recrystallized grain size and Zener-Holloman parameter (Z) in Mg-alloys as follows:

$$\frac{D_f}{D_0} = 10^3 Z^{-1/3} = 10^3 [\dot{\epsilon} \exp^{Q/RT}]^{-1/3} \quad (4)$$

The estimated strain rate and maximum temperature experienced by FS processed composites were 30.5 s<sup>-1</sup>, and 295 °C, respectively as per the model reported in Ref. [32]. The average grain size of as-cast PL700 specimen was found to be 50 μm. After incorporating all these numerical values into the Eq. (4), the estimated grain size due to DRX in FPL700 was 1.5 μm. Calculated recrystallized grain size is nearly in consistent with the current experimental data (the average grain size of FPL700 specimen is 2.5 μm). Further, the presence of PDC particles in the Mg matrix also accelerates the DRX kinetics due to two reasons: Firstly, particles generate higher density of dislocations within the matrix due to mismatch in coefficient of thermal expansion prior to FSP treatment. Thus pre-existence of dislocations eventually provides stored energy to initiate DRX process. Secondly, the nano-sized PDC particles suppress any abnormal grain growth due to Zener pinning effect during FSP [33].

### 5.3. Mechanical properties

Hardness of FS processed composites is significantly higher compared to that of as-cast composites irrespective of the process temperatures (Fig. 10). For instance, the hardness values of FPL800 and FPL700 specimens are enhanced by 45% and 95% as compared to that of the as-cast PL800 and PL700 specimens, respectively. Such increases in hardness could be attributed to significant refinement of both the grain size of the matrix material, and size of the PDC particles caused by FSP. Further, FSP minimizes the grain boundary segregation of PDC particles due to their uniform dispersion throughout the Mg matrix. As there is a slight difference in volume fraction of reinforced PDC particles between PL800 and PL700 specimens due to the formation of Mg<sub>2</sub>Si particles in PL800 specimen, and this has led to marginal variation in their hardness (Fig. 10). Compressive true stress-true strain plots show that yield strengths and ultimate compressive strengths (UCS) of FS processed composites are higher compared to that of their as-cast counterparts as seen in Fig. 11(a). For instance, the yield strength and UCS of FL700 specimen is enhanced by 158% and 125%, respectively. The increase in yield strength of FS processed composites stems from contribution of various strengthening mechanisms as discussed later. Another striking difference in compression data is the level of strain to failure (ε<sub>f</sub>) among the processed composites. For instance, the value of ε<sub>f</sub> in as-cast PL800 was found to be only 10% whereas it was increased by 80% after FSP. The emergence of lower ε<sub>f</sub> (10%) for as-cast PL800 specimen could be associated with the presence of dendritic Mg<sub>2</sub>Si crystal which acts as stress raiser to accelerate damage accumulation in the composites. It is to be noted that the as-cast PL700 specimen exhibits reasonable ε<sub>f</sub> (18%) due to reduced Mg<sub>2</sub>Si formation at 700 °C. The increase in the value of ε<sub>f</sub> for FL800 specimen could be ascribed to simultaneous refinement in the grain size of the Mg matrix as well as the PDC particles. Further, the value of ε<sub>f</sub> for as-cast PL700 and FPL700 specimen are measured to be 18% and 22% respectively. The FPL700 specimen shows marginal increment in the value of ε<sub>f</sub> by 22%, and this indicates that ductility is retained even though yield stress is higher. Strain hardening exponent determines how well the composites work harden with the imposed applied stress. Fig. 11(b) shows that FS processed PL700 composites exhibits highest strain hardening exponent amongst all the composites processed. The strain hardening exponent is estimated from the constitutive equation of true stress-true strain relation as follows:

$$\sigma = K \epsilon^n \quad (5)$$

where σ, ε, K, and n are the true stress, true strain, strength coefficient, and strain hardening exponent, respectively. By taking logarithm on

**Table 1**  
Summary of mechanical properties in Mg-based in-situ composites.

Composites	Micro-hardness (HV0.5)	Compressive yield stress (CYS), MPa	Ultimate compressive strength (UCS), MPa	Strain to failure %	Strain hardening exponent
As cast PL800	53 ± 2	90 ± 5	190 ± 11	10 ± 1.0	0.25 ± 0.04
As cast PL700	44 ± 2	85 ± 3	235 ± 7	18 ± 0.5	0.30 ± 0.03
FS processed PL800	77 ± 3	205 ± 6	395 ± 20	18 ± 0.8	0.35 ± 0.02
FS processed PL700	86 ± 1	220 ± 5	530 ± 21	22 ± 0.5	0.45 ± 0.02

both sides of the Eq. (5), and then rearranging into the following form

$$\text{Log}(\sigma) = \text{Log}(K) + n \text{Log}(\epsilon) \quad (6)$$

The values of strain hardening exponent (n) is determined from the plot of compression data as Log(σ) vs. Log(ε). For estimating “n” values, slope in the plastic strain region (corresponding to true strain in the range of 0.05–0.10) of true stress-true strain curves is considered. As strain hardening exponent is more closely related to the density of dislocations prior to plastic deformation, it would be appropriate to discuss this trend along with Taylor strengthening effect. The summary of mechanical properties of all the composites studied here is provided in Table 1.

Basically, yield strength of the particulate MMCs can be enhanced by four different strengthening modes [34] namely: (i) Hall-Petch effect (ii) Orowan mechanism (iii) Taylor contribution and (iv) load transfer strengthening. These strengthening mechanisms are summarized in Table 2. The properties and parameters which were used for estimating the contribution of strengthening modes are provided in Table 3. After assessing different strengthening mechanisms, Hall-Petch mechanism was found to be the major strength enhancement contributor in both the as-cast and FS processed composites (Fig. 12(a)). The activation of Hall-Petch effect in the processed composites (both as-cast and FS processed condition) can be explained as follows. For the case of as-cast composites, the presence of PDC particles in the molten Mg served as heterogeneous nucleation sites and help in the nucleation of Mg grains. In addition, the grain boundary segregation of PDC particles restricts the grain growth during solidification. Both these factors contribute to considerable refinement in the grain size leading to operation of Hall-Petch effect. For instance, the average grain size of the as-cast composites is typically in the range of 50–65 μm, while it was 410 ± 25 μm for the case of unreinforced pure magnesium. After single-pass FS processing of these as-cast composites, the mean grain size is reduced further from 50 μm to 2.5 μm. As mentioned earlier, DRX process appears to be the major contributing factor in the grain refinement. Finer the grain size, higher the chance of impeding the dislocation motion at the grain boundaries which eventually leads to

**Table 2**  
Summary of various strengthening mechanisms.

Strengthening models	Mechanisms	Governing equations
Hall-Petch	Interaction of dislocations at the grain boundaries	$\Delta\sigma_{HP} = K_{HP} [D_f^{-1/2} - D_o^{-1/2}]$
Orowan	Formation of Orowan loops around reinforced particles	$\Delta\sigma_{Orowan} = \frac{\beta G_m b}{d_p} \left[ \frac{6V_f}{\pi} \right]^{1/3}$
Taylor	Dislocation enrichment due to thermal mismatch between matrix and reinforced particles	$\Delta\sigma_{Taylor} = \sqrt{3} \rho G_m b \left[ \frac{12V_f \Delta\alpha \Delta T}{b(1 - V_f)d_p} \right]^{1/2}$
Load bearing	Load transfer from soft matrix to hard particles	$\Delta\sigma_{LT} = \frac{1}{2} \sigma_{ym} V_f$

**Table 3**  
Important physical and mechanical properties used in the strengthening models.

Properties or parameters	In-situ Composites			
	PL700	PL800	FPL700	FPL800
Hall-Petch Coefficient of the matrix (Mg)	0.280			
Shear modulus of the matrix (Mg), GPa	16.5			
Poisson ratio of the matrix (Mg)	0.35			
Burger vector of the matrix (Mg), nm	0.32			
Thermal expansion coefficient of the matrix (Mg) × 10 <sup>-6</sup> μK <sup>-1</sup>	26.5			
Thermal expansion coefficient of SiCNO × 10 <sup>-6</sup> μK <sup>-1</sup>	3.5			
Thermal expansion coefficient of Mg <sub>2</sub> Si crystals × 10 <sup>-6</sup> μK <sup>-1</sup>	7.5			
Yield strength of the matrix (Mg), MPa	60 ± 3			
Yield strength of composites, MPa	85	90	220	205
Process Temperature, K	973	1073	973	1073
Mean grain size before reinforcement incorporation, μm	410 ± 25			
Mean grain size of the composites, μm	50 ± 2	65 ± 3	2.5 ± 0.2	3.5 ± 0.3
Size of the SiCNO particles, nm	500–1000		200–300	
Size of the Mg <sub>2</sub> Si crystals, μm	– 200		– 50	
Volume fraction of SiCNO	0.025	0.020	0.025	0.020
Volume fraction of Mg <sub>2</sub> Si crystals	– 0.10		– 0.10	

increase in the contribution of Hall-Petch strengthening. Next, Taylor strengthening plays a major role in enhancing yield strength of MMCs, if there is a considerable temperature difference (ΔT) between the process, and test condition. If composite is subjected to heating or cooling, the differences in coefficients of thermal expansion (CTE) between matrix material and reinforced particles shall produce a thermal strain and internal stress state changes. In order to accommodate this thermal mismatch effect, dislocations are generated around reinforced particles within the matrix material. The magnitude of thermal strain (Δε<sub>T</sub> = ΔαΔT) determines the density of dislocations generated within the composites. The thermal expansion mismatch (Δα) between the Mg matrix and SiCNO particles is = 23 × 10<sup>-6</sup> (K<sup>-1</sup>). Similarly the thermal expansion mismatch between the Mg matrix and Mg<sub>2</sub>Si crystals is 19 × 10<sup>-6</sup> (K<sup>-1</sup>). This huge CTE mismatch leads to enhanced dislocation density in the magnesium matrix. Higher the density of dislocations, lesser the mean free path distance travelled by a moving dislocation which eventually tending to enhance the contribution of Taylor strengthening. It is well-known fact that the contribution of Taylor strengthening decreases with reduction in ΔT. This should be reflected when processing changes from liquid-state (casting) to solid-state (FSP). For instance, ΔT for casting process is 673 K whereas it is only 268 K for FSP. However, both as-cast and FS processed composites exhibit more or less similar magnitude of Taylor strengthening as seen in Fig. 12(a). Influence of ΔT is eliminated by the refinement of PDC particles during FSP. In fact, Taylor equation explicitly demonstrates that fine-sized particle can generate more number of dislocations as compared to large particles (Table 2). Even if one assumes FS processed composites possess negligible amount of dislocations, geo-

**Table 4**  
Summary of numerical models to estimate yield strength.

Numerical models	Equations
Summation Zhang and Chen	$\Delta\sigma_S = \sigma_{ym} + \Delta\sigma_{Taylor} + \Delta\sigma_{LT} + \Delta\sigma_{Orowan} + \Delta\sigma_{HP}$ $\Delta\sigma_{ZC} = (1 + 0.5V_f) \left[ \sigma_{ym} + \Delta\sigma_{Orowan} + \Delta\sigma_{Taylor} + \left( \frac{\Delta\sigma_{Orowan} \Delta\sigma_{Taylor}}{\sigma_{ym}} \right) \right]$
Modified Clyne	$\Delta\sigma_{MC} = \sigma_{ym} + \sqrt{(\Delta\sigma_{Taylor})^2 + (\Delta\sigma_{LT})^2 + (\Delta\sigma_{Orowan})^2 + (\Delta\sigma_{HP})^2}$

metric necessary dislocations (GNDs) come into action to enhance yield strength during plastic deformation. The contribution of GND component is assumed to be negligible since it overestimates yield strength of composites in the present work. The increase in strain hardening exponents also confirmed the existence of Taylor strengthening in FS processed composites. The Orowan strength is mainly determined by dispersed particles being able to impede the movement of dislocation. Orowan strength inversely proportional to the mean inter-particle spacing between the dispersed particles. Therefore, the intensity of dislocation trapping by dispersed ceramic particles (i.e contribution of Orowan strengthening) increases with decreasing their particle size. Further the degree of uniformity in the dispersion of PDC particles within the Mg matrix was also enhanced significantly by FSP. Therefore, the contribution of Orowan strengthening is enhanced in FS processed composites especially in FPL700 specimen due to refinement of PDC particles by FSP. For instance, the contribution of Orowan strength is increased up to 14 MPa for FPL700 specimen while it was only 3 MPa in the as-cast composites. It is obvious that load transfer strengthening loses its importance in yield strength contribution due to lower volume fraction of the PDC particles as seen in Fig. 12(a).

### 5.3.1. Verification of the numerical models

The most common numerical models to quantify the total yield strength of particulate MMCs [35] are as follows: (i) the simple summation model which adds up all the strengthening contributions by assuming that each mechanism behaves individually (ii) Zhang and Chen model is a modified version of shear-lag model which considers the effects of Orowan, Taylor and load transfer strengthening but neglects the contribution of Hall-Petch effect [36] and (iii) modified Clyne model includes the effects of all strengthening mechanisms which act unevenly by least-square approximation. The governing equations for these numerical models are provided in the Table 4. Sanaty-Zadeh et al. [35] reported that the modified Clyne method can predict the yield strength more precisely than any other methods after comparing the various numerical models for the particulate MMCs. Fig. 12(b) shows that while the Zhang and Cheng model underestimates the yield strength of FS processed composites and the summation model overestimates the yield strengths of all the composites irrespective of processing conditions. However, the agreement between yield strength of composites predicted by modified Clyne model and experimental method appears to be reasonably good for both the as-cast as well as FS processed composites as seen in Fig. 12(b). The reason for underestimation by Zhang and Cheng model is that it neglects the contribution of Hall-Petch effect brought out by FSP. It is to be noted that if the contribution of Taylor strengthening is equivalent to that of Hall-Petch strengthening, then there occurs no significant deviation from the experimental values even with Zhang and Chen model. In other words, the Zhang and Chen model loses its precision only if there is huge contribution from Hall-Petch effect. Overestimation of yield strength by summation model indicates that no strengthening mechanism can act individually and should depend on each other irrespective of processing condition. In summary, we have explored two-step processing to address the existing disadvantages associated with primary processing of Mg-based in-situ MMCs derived

from polymer precursor approach. The intensity of formation of Mg<sub>2</sub>Si phase, and grain boundary segregation of reinforced PDC particles were minimized if processing of in-situ composites are done at 700 °C and followed by FSP processing. Two-step process can be employed to enhance the performance of light weight Mg-based in-situ MMCs for automotive and structural applications.

## 6. Conclusions

1. In-situ magnesium matrix composites containing nano-sized SiCNO particles are fabricated by combining both the liquid- and solid-state processing routes. Liquid-state process helps to produce in-situ ceramic particles via pyrolysis of liquid polymer, while solid-state FSP aids in improving the uniformity of particle distribution, minimizing segregation, particle refinement, and refinement of grain sizes of composites.
2. During in-situ pyrolysis, it is possible to minimize the formation of Mg<sub>2</sub>Si phase by reducing the processing temperature from 800 °C to 700 °C.
3. Micro-hardness, yield stress, ultimate compressive stress, strain to failure and strain hardening exponent of the as-cast composites are improved by 95%, 158%, 125%, 22% and 50% respectively after FSP. Two-stage processed composites pyrolysed at 700 °C exhibits uniform reinforced particle distribution and superior mechanical properties as compared to any other composites.
4. Hall-Petch strengthening was found to be the most dominant mechanism on enhancing the yield strength of Mg-based in-situ MMCs processed by two-stage process. This could be explained due to the occurrence of DRX during FSP. Modified Clyne model fits well with experimental data of yield strength of the composites as compared to Zhang and Chen and summation models.

## Acknowledgement

The authors would like to express their gratitude to Prof. Rishi Raj, University of Colorado, Boulder, for his valuable inputs, and for providing the precursor materials under Grant No. DMR1105347 supported by the National Science Foundation. The authors would like to convey special thank to Dr. Padaikathan, IISc Bangalore for his extensive help in TEM characterization. The authors would also like to acknowledge Mr. Ram Kumar, Mr. Juljeet Singh and Mr. Amit Kaushal, for their help in casting, friction stir processing experiments and XRD characterization respectively.

## Appendix. (Notations):

The following symbols are used in the present paper:

$W_f^P$	weight fraction of liquid polymer
$\rho_{PDC}$	theoretical density of PDC particles
$\rho_{Mg}$	theoretical density of pure magnesium
$V_f^{PDC}$	projected volume fraction of PDC particles, and
$D_f$	mean grain size of the final matrix

$D_0$	mean grain size of the original matrix
$Z$	Zener-Holloman parameter
$\dot{\epsilon}$	strain rate
$Q$	activation energy for lattice diffusion
$R$	universal gas constant
$T$	temperature
$\Delta\sigma_{HP}$	enhancement in yield strength by Hall-Petch effect
$K_{HP}$	Hall-Petch coefficient
$\Delta\sigma_{OR}$	enhancement in yield strength by Orowan effect
$\beta$	numerical constant
$G_m$	shear modulus of the matrix
$b$	Burger vector of the matrix,
$d_p$	mean diameter of the reinforced particles
$V_f$	volume fraction of the reinforced particles
$\Delta\sigma_{LT}$	enhancement in yield strength by load bearing effect
$\sigma_{ym}$	enhancement in yield strength by Taylor effect
$\Delta\sigma_{Taylor}$	enhancement in yield strength by Taylor effect
$\varphi$	Taylor factor
$\Delta\alpha$	thermal mismatch difference between matrix and reinforcement
$\Delta T$	temperature difference between process and test
$\Delta\sigma_s$	enhancement in yield strength by summation
$\Delta\sigma_{ZC}$	enhancement in yield strength by Zhang and Chen model
$\Delta\sigma_{LT}$	enhancement in yield strength by modified Clyne model
$\sigma$	yield strength or true stress
$\epsilon$	True strain
$n$	strain hardening exponent
$K$	strength coefficient
$\epsilon_f$	Strain to failure

## References

- [1] B.L. Mordike, T. Ebert, Magnesium properties-applications-potential, *Mat. Sci. Engg: A* 302 (2001) 37–45.
- [2] H. Friedrich, S. Schumann, Research for a new age of magnesium in the automotive industry, *J. Mater. Proc. Tech.* 117 (2001) 276–281.
- [3] J. Hashim, L. Looney, M.S.J. Hashmi, Metal matrix composites: production by the stir casting method, *J. Mater. Proc. Tech.* 92–93 (1999) 1–7.
- [4] H. Hu, Squeeze casting of magnesium alloys and their composites, *J. Mater. Sci.* 33 (1998) 1579–1589.
- [5] S.C. Tjong, Z.Y. Ma, Microstructural and mechanical characteristics of in-situ metal matrix composites, *Mater. Sci. Engg: R* 29 (2000) 49–113.
- [6] H.Y. Wang, Q.C. Jiang, X.L. Li, J.G. Wang, Q.F. Guan, H.Q. Liang, In situ synthesis of TiC from nanopowders in a molten magnesium alloy, *Mat. Res. Bull.* 38 (2003) 1387–1392.
- [7] P. Bhingole, G.P. Chaudhari, S.K. Nath, Processing, microstructure and properties of ultrasonically processed in-situ MgO-Al<sub>2</sub>O<sub>3</sub>-MgAl<sub>2</sub>O<sub>4</sub> dispersed magnesium alloy composites, *Comp. A: Appl. Sci. Manuf.* 66 (2014) 209–217.
- [8] K. Kondoh, H. Oginuma, A. Kimura, S. Matsukawa, T. Aizawa, In-situ synthesis of Mg<sub>2</sub>Si intermetallics via powder metallurgy process, *Mater. Trans.* 44 (2003) 981–985.
- [9] Q. Dong, L.Q. Chen, M.J. Zhao, J. Bi, Synthesis of TiCp reinforced magnesium matrix composites by in-situ reactive infiltration process, *Mater. Lett.* 58 (2004) 920–926.
- [10] M. Shamekh, M. Pugh, M. Medraj, Understanding the reaction mechanism of in-situ synthesized (TiC–TiB<sub>2</sub>)/AZ91, *Magnesium Matrix Compos. Mat. Chem. Phys.* 135 (2012) 193–205.
- [11] Sudarshan, M.K. Surappa, Dongjoon Ahn, Rishi Raj, Nanoceramic-metal matrix composites by in-situ pyrolysis of organic precursors in a liquid melt, *Met. Mater. Trans. A* 39 (2008) 3291–3297.
- [12] Sudarshan, A.R. Terauds, Anil Chandra, Rishi Raj, Polymer-derived in-situ metal matrix composites created by direct injection of liquid polymer into molten magnesium, *Met. Mater. Trans: A* 45 (2014) 551–554.
- [13] M.K. Surappa, Microstructural evolution during solidification of DRMMCs (Discontinuous reinforced metal matrix composites): state of art, *J. Mater. Proc. Tech.* 63 (1997) 325–333.
- [14] T.S. Srivatsan, T.S. Sudarshan, E.J. Lavernia, Processing of discontinuously-reinforced metal matrix composites by rapid solidification, *Prog. Mater. Sci.* 39 (1995) 317–409.
- [15] M. Gupta, M. Lai, D. Saravanaranganathan, Synthesis, microstructure and properties characterization of disintegrated melt deposited Mg/SiC composites, *J. Mater. Sci.* 35 (2000) 2155–2165.
- [16] S. Roy, G. Kannan, S. Suwas, M.K. Surappa, Effect of extrusion ratio on the microstructure, texture and mechanical properties of (Mg/AZ91) m–SiC p composite, *Mater. Sci. Engg: A* 624 (2015) 279–290.
- [17] R.S. Mishra, Z.Y. Ma, Friction stir welding and processing, *Mat. Sci. Engg: R* 50 (2005) 1–78.
- [18] H. Arora, H. Singh, B.K. Dhindaw, Some observations on microstructural changes in a Mg-based AE42 alloy subjected to friction stir processing, *Met. Mat. Trans: B* 43 (2012) 92–108.
- [19] Ranjit Bauri, Optimization of process parameters for friction stir processing (FSP) of Al–TiC in situ composite, *Bull. Mater. Sci.* 37 (2014) 571–578.
- [20] A. Kumar, R. Raj, S.V. Kailas, novel in-situ polymer derived nano ceramic MMC by friction stir processing, *Mater. Des.* 85 (2015) 626–634.
- [21] Y.L. Li, E. Kroke, R. Reidel, C. Fasel, C. Gervais, F. Babanneau, Thermal cross-linking and pyrolytic conversion of poly(ureamethylvinyl)silazanes to silicon-based ceramics, *App. Organomet. Chem.* 15 (2001) 820–832.
- [22] E. Kroke, Y.L. Li, C. Konetschny, E. Lecomte, C. Fasel, R. Riedel, Silazane derived and related materials, *Mater. Sci. Eng: R* 26 (2003) 197–199.
- [23] X. Yuan, W. Sun, Y. Du, D.D. Zhao, H. Yang, Thermodynamic modeling of the Mg–Si system with the Kaptay equation for the excess Gibbs energy of the liquid phase, *Calphad* 33 (2009) 673–678.
- [24] B. Inem, G. Pollard, Interface structure and fractography of a magnesium-alloy, metal-matrix composite reinforced with SiC particles, *J. Mater. Sci.* 28 (1993) 4427–4434.
- [25] C.J. Lee, J.C. Huang, P.J. Hsieh, Mg based nano-composites fabricated by friction stir processing, *Scr. Mater.* 54 (2006) 1415–1420.
- [26] V.M. Borshchev, A.N. D'yachenko, A.D. Kiselev, R.I. Kraidenko, Production of silicon from magnesium silicide, *Russ. J. Appl. Chem.* 86 (2013) 493–497.
- [27] Y.S. Sato, H. Kokawa, M. Enmoto, S. Jogan, Microstructural evolution of 6063 aluminum during friction-stir welding, *Metall. Mat. Trans: A* 30 (1999) 2429.
- [28] W.B. Lee, C.Y. Lee, M.K. Kim, J.I. Yoon, Y.J. Kim, Y.M. Yoen, S.B. Jung, Microstructures and wear property of friction stir welded AZ91 Mg/SiC particle reinforced composite, *Compos. Sci. Technol.* 66 (2006) 1513–1520.
- [29] A.H. Feng, Z.Y. Ma, Microstructural evolution of cast Mg–Al–Zn during friction stir processing and subsequent aging, *Acta Mater.* 57 (2009) 4248–4260.
- [30] T.R. McNelley, S. Swaminathan, J.Q. Su, Recrystallization mechanisms during friction stir welding/processing of aluminum alloys, *Scr. Mater.* 58 (2008) 349–354.
- [31] H. Watanabe, H. Tsutsui, T. Mukai, H. Ishikawa, Y. Okanda, M. Kohzu, K. Higashi, Grain size control of commercial wrought Mg–Al–Zn Alloys utilizing dynamic recrystallization, *Mat. Trans.* 42 (2001) 1200–1205.
- [32] C.I. Chang, C.J. Lee, J.C. Huang, Producing nanograined microstructure in Mg–Al–Zn alloy by two-step friction stir processing, *Scr. Mater.* 51 (2004) 509.
- [33] C.I. Chang, Y.N. Wang, H.R. Pei, C.J. Lee, J.C. Huang, On the Hardening of Friction Stir Processed Mg–AZ31 Based Composites with 5–20% Nano-ZrO<sub>2</sub> and Nano-SiO<sub>2</sub> Particles, *Mater. Trans.* 47 (2006) 2942–2949.
- [34] S.C. Tjong, Novel nanoparticle-reinforced metal matrix composites with enhanced mechanical properties, *Adv. Eng. Mater.* 9 (2007) 639–652.
- [35] A. Sanaty-Zadeh, P.K. Rohatgi, Comparison between current models for the strength of particulate-reinforced metal matrix nanocomposites with emphasis on consideration of Hall-Petch effect, *Mater. Sci. Eng. A* 531 (2012) 112–118.
- [36] Z. Zhang, D.L. Chen, Contribution of Orowan strengthening effect in particulate-reinforced metal matrix nanocomposites, *Mater. Sci. Eng: A* 483–484 (2008) 148–152.